



Alessandro Ciallella · Francesco D'Annibale ·
Dionisio Del Vescovo · Ivan Giorgio

Deformation patterns in a second-gradient lattice annular plate composed of “*Spira mirabilis*” fibers

Received: 12 October 2022 / Accepted: 3 November 2022
© The Author(s) 2022

Abstract In this paper, we aim to explore the mechanical potentialities of a material made of an orthogonal net of fibers arranged in logarithmic spirals. Therefore, an annular plate described with a second-gradient model is envisaged to evaluate the behavior of such material in a nonlinear elastic regime when large displacements and deformations occur. Several mechanical tests are performed numerically under the finite element method approximation obtained directly with a weak formulation based on the elastic energy that it is assumed to be predictive for this kind of network system of fibers. Plots reporting the mechanical characteristics in all the considered tests are provided to illustrate the overall mechanical behavior of the evaluated system.

Keywords Nonlinear elasticity · Second-gradient surfaces · Homogenized nets · Metamaterials

1 Introduction

Spira mirabilis, i.e., the marvelous spiral, as the mathematician Jakob Bernoulli named the logarithmic spiral, is a motif somewhat recurring in nature. Many examples of structures organized with this shape can be found indeed. For instance, structures approximately similar to the logarithmic spiral might be recognized in some shells of many mollusks. It is no coincidence that in some topological optimizations, an arrangement of the material following these curves is obtained, as shown by some results obtained after the frequently cited work of the mechanical engineer Anthony G. M. Mitchell [1]. These last results can be used as the starting point

Communicated by Andreas Öchsner.

Francesco D'Annibale, Dionisio Del Vescovo, and Ivan Giorgio have contributed equally to this work.

A. Ciallella · F. D'Annibale · I. Giorgio (✉)
Department of Civil, Construction-Architectural and Environmental Engineering (DICEAA), University of L'Aquila,
P.zza Ernesto Pontieri 1, Monteluco di Roio, 67100 L'Aquila, Italy
E-mail: ivan.giorgio@univaq.it

A. Ciallella
E-mail: alessandro.ciallella@univaq.it

F. D'Annibale
E-mail: francesco.dannibale@univaq.it

A. Ciallella · F. D'Annibale · D. Del Vescovo · I. Giorgio
International Research Center for the Mathematics and Mechanics of Complex Systems (M&MoCS), University of L'Aquila,
P.zza Ernesto Pontieri 1, Monteluco di Roio, 67100 L'Aquila, Italy
E-mail: dionisio.delvescovo@uniroma1.it

D. Del Vescovo
Department of Mechanical and Aerospace Engineering (DIMA), University of Rome La Sapienza, via Eudossiana 18,
00184 Rome, Italy

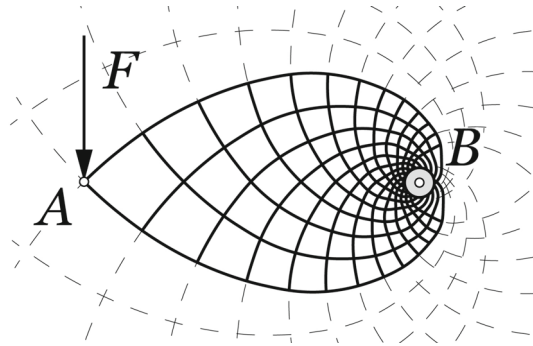


Fig. 1 Michell's cantilever truss

for designing a net of curved fibers. The mechanics of elastic networks made of fibers is a challenging and fruitful topic since the pioneering works of Tchebychev on nets composed of inextensible fibers [2]. Systems constituted by an orthogonal network of fibers lying on a plane that can deform, while remaining embedded onto a surface could be conceived for many engineering applications as well as regarded as the reinforcement in a composite material. Especially nowadays, having at our disposal 3D printing technology [3–11], it is possible to build curved fiber networks optimized for many demanding tasks. In this paper, stepping in Mitchell's footprints, we analyze a network of fibers arranged following logarithmic spirals (see [1] and later on [12]). The key idea for Mitchell is to find optimal “frame structures” to attain as much as possible the limit of the material economy under considered applied actions. This result can be accomplished, for small deformations, if the lengths in all the bars of the frame increase by equal fractions but not less than the fractional change of length of any element of the space occupied by the frame. In this context, Mitchell's frames are truss systems of bars where they are arranged in orthogonal systems of curves both before and after the deformation. Among the solutions proposed by Mitchell is the case of a perpendicular network of curves made of logarithmic spirals (see Fig.1).

An efficient way to model this kind of network systems consists in employing equivalent continuum elastic models based on strain-gradient [13–20], micro-morphic [21–26], or micro-polar [27–32] theories. In this paper, we adopt a second-gradient model that is able to describe the storage of elastic energy of a continuous distribution of fibers with several mechanisms of deformations. Specifically, we consider (1) the elongations of fibers, (2) a macroscopic shear deformation related to a change in the angle between the fibers connected to each other, (3) their curvature related to a deformation in the tangent plane to the net as well as for the out-of-plane bending and, finally, (4) the twisting of the fibers. Herein, we aim to characterize this kind of 2D material from a mechanical point of view. The cantilever truss proposed by Mitchell can be generalized by conceiving a polar symmetric prototype to fit a broader range of applications. With this intent, we consider an annular plate made with this arrangement of fibers and investigate its mechanical responses using numerically executed tests.

2 The model

2.1 Second-gradient sheet made by a fiber net

In this section, a bidimensional and second-gradient continuum model, embedded in the 3D space, for a net of curved fibers lying on a plane is described. First, the general framework is recalled. Then, it is specialized for a net made of orthogonal fibers disposed along logarithmic spirals [33–38]. This model is based on the following assumptions: (i) The homogenized surface is made of an infinite distribution of two families of fibers; (ii) for every fiber, the shear deformation is negligible; therefore, all the fiber cross-sections remain orthogonal to the tangent vector to the middle line of the fiber in the current configuration; (iii) the intersection points between the two families of the fibers constituting the network share the same position in any configuration, namely no relative motions are allowed at these points; (iv) the only degree of freedom permitted at these intersection points is a relative rotation of the fiber cross sections with respect to the orthogonal vector to the current tangent plane generated as the span of the two tangent vectors at the middle lines of the two fiber families. The considered elastic surface, \mathcal{S} , is represented by means of the positions in the current configuration, $\mathbf{x} = (x_1, x_2, x_3) \in \mathbb{R}^3$, of the material points defining the reference configuration, $\mathbf{X} = (X_1, X_2) \in \Omega \subset \mathbb{R}^2$.

The map χ that links the reference configuration X and the current one \mathbf{x} , through the displacement vector of components u_i , is:

$$\mathbf{x} = \chi(X) = X_\alpha \mathbf{e}_\alpha + u_i(X) \mathbf{e}_i \quad (1)$$

in which Greek indexes range from 1 to 2, while Latin ones from 1 to 3. Einstein's convention is adopted for both of them, and the unit vectors $\{\mathbf{e}_i\}$ define the basis used to describe the surface \mathcal{S} . The central lines of the fibers are described by a parametric representation in the framework of a Lagrangian description using the two 'material' abscissae S_β ($\beta = 1, 2$) in the reference configuration as $X = X(S_\beta)$. In the case in which S_β characterizes a unit-speed parametrization, the tangent vectors to the fibers in the reference configuration are of norm one and can be expressed as

$$\mathbf{D}_\beta(X) = \frac{dX_\alpha}{dS_\beta} \mathbf{e}_\alpha \quad (2)$$

The tangent vectors in the current configuration are instead given by

$$\lambda_\beta(X) \mathbf{d}_\beta(X) = \frac{d\chi}{dS_\beta}(X) = \mathbf{F}(X) \mathbf{D}_\beta(X) \quad (3)$$

where $\lambda_\beta = \|\mathbf{F} \mathbf{D}_\beta\|$, $\mathbf{F} = \nabla_X \chi$, that is the deformation gradient tensor, which is represented by a 3×2 matrix, and \mathbf{d}_β are the unit fiber tangent vectors in the current configuration. The unit vector orthogonal to the surface \mathcal{S} is

$$\mathbf{n}(X) = \frac{\mathbf{d}_1 \times \mathbf{d}_2}{\|\mathbf{d}_1 \times \mathbf{d}_2\|} \quad (4)$$

which can be simplified as

$$\mathbf{n}(X) = \frac{\varepsilon_{ijk} F_{j2} F_{k1} \mathbf{e}_i}{\|\varepsilon_{ijk} F_{j2} F_{k1} \mathbf{e}_i\|} \quad (5)$$

when the fibers in the reference configuration are orthogonal ($\mathbf{D}_1 \cdot \mathbf{D}_2 = 0$); ε_{ijk} stands for the Levi-Civita symbol.

In the framework of Kirchhoff's model of rods [39–43], the cross-section orientation of fibers can be described by a rotation tensor as follows:

$$\mathbf{R}_\beta : \{\mathbf{e}_i\} \mapsto \{\mathbf{d}_\beta, \mathbf{n} \times \mathbf{d}_\beta, \mathbf{n}\} \quad (6)$$

and, consequently, the curvature tensor can be given by

$$\mathbf{W}_\beta = \mathbf{R}_\beta^\top \frac{d\mathbf{R}_\beta}{dS_\beta} \quad (7)$$

which is a skew-symmetric tensor whose significant components are the twisting, the out-of-plane curvature, and the geodesic one, namely

$$\kappa_{T\beta} = (\mathbf{n} \times \mathbf{d}_\beta) \cdot \frac{d\mathbf{n}}{dS_\beta}, \quad \kappa_{n\beta} = \mathbf{n} \cdot \frac{d\mathbf{d}_\beta}{dS_\beta}, \quad \kappa_{g\beta} = -(\mathbf{n} \times \mathbf{d}_\beta) \cdot \frac{d\mathbf{d}_\beta}{dS_\beta}, \quad (8)$$

respectively. The differentiation with respect to the curvilinear abscissa S_β gives

$$\frac{d\mathbf{d}_\beta}{dS_\beta} = \frac{1}{\lambda_\beta} [\nabla_X \mathbf{F} | \mathbf{D}_\beta \otimes \mathbf{D}_\beta + \mathbf{F} (\nabla_X \mathbf{D}_\beta \mathbf{D}_\beta)] - \frac{d\lambda_\beta}{dS_\beta} \frac{\mathbf{d}_\beta}{\lambda_\beta} \quad (9)$$

where the above-mentioned expressions are evaluated by

$$\begin{aligned} (\nabla_X \mathbf{F} | \mathbf{D}_\beta \otimes \mathbf{D}_\beta)_i &= \frac{\partial F_{i\alpha}}{\partial X_\eta} (\mathbf{D}_\beta)_\eta (\mathbf{D}_\beta)_\alpha \\ (\nabla_X \mathbf{D}_\beta \mathbf{D}_\beta)_\alpha &= \frac{d^2 X_\alpha}{dS_\beta^2}. \end{aligned}$$

The derivative of \mathbf{n} with respect to S_β can be performed from Eq. (4). The measures of deformation used to describe the behavior of the elastic surface \mathcal{S} incorporating the effects due to the fibers are therefore:

1. The *fiber stretching*

$$\varepsilon_\beta = \lambda_\beta - 1 \quad (10)$$

2. The *shear distortion angle*

$$\gamma = \text{asin}(\mathbf{d}_1 \cdot \mathbf{d}_2) \quad (11)$$

3. The *curvature change*

$$\Delta\kappa_{T\beta} = \kappa_{T\beta} - \kappa_{T\beta}^0, \quad \Delta\kappa_{n\beta} = \kappa_{n\beta} - \kappa_{n\beta}^0, \quad \Delta\kappa_{g\beta} = \kappa_{g\beta} - \kappa_{g\beta}^0 \quad (12)$$

where the superscript ‘0’ refers to the reference configuration.

In the case of a planar surface in the reference configuration, $\kappa_{T\beta}^0 = 0$ and $\kappa_{n\beta}^0 = 0$, the geodesic curvature can be evaluated as follows:

$$\kappa_{g\beta}^0 = -(\mathbf{e}_3 \times \mathbf{D}_\beta) \cdot \frac{d\mathbf{D}_\beta}{dS_\beta} \quad (13)$$

The elastic energy of the considered surface is assumed to be

$$\begin{aligned} 2U[\chi(\cdot)] &= \int_\Omega \sum_{\beta=1}^2 K_{e\beta} (\lambda_\beta - 1)^2 d\Omega + \int_\Omega K_s \gamma^2 d\Omega \\ &+ \int_\Omega \sum_{\beta=1}^2 K_{g\beta} (\kappa_{g\beta} - \kappa_{g\beta}^0)^2 d\Omega + \int_\Omega \sum_{\beta=1}^2 K_{n\beta} (\kappa_{n\beta})^2 d\Omega \\ &+ \int_\Omega \sum_{\beta=1}^2 K_{T\beta} (\kappa_{T\beta})^2 d\Omega \end{aligned} \quad (14)$$

where $K_{e\beta}$, K_s , $K_{g\beta}$, $K_{n\beta}$, and $K_{T\beta}$ are the significative stiffnesses for the two families of fibers, namely related to stretching, shearing, geodesic and normal bending, and twisting, respectively.

2.2 Logarithm spiral lattices

A net of orthogonal fibers disposed along logarithmic spirals is now considered and analyzed numerically with the aim of illustrating its mechanical responses in view of potential applications. The fibers are connected to each other through cylindrical pivots [44–46] that behave as deformable hinges to provide a relative motion between the fibers. This type of connection is able to provide a sufficiently yielding link that can satisfy the hypothesis *iv* stated in Sect. 2. A prototype that fits this description is shown in Fig. 2. Nowadays, since the enormous progress made by 3D printing technology, it is increasingly easy to conceive and produce complex substructures that can provide significant resistance with a limited amount of material. The system under study falls in that line of research.

In what follows, a representative sample is considered. It is made of fibers with a rectangular cross section of size $b \times h$, namely the base $b = 1.6$ mm and the height $h = 1$ mm. They are connected through cylindrical pivots having radius $r_p = 0.45$ mm and height $h_p = 1$ mm. In the examined case, the middle lines of the fibers are represented by the two families of curves

$$\begin{cases} X_1 = R_0 e^{(\varphi+\psi)} \cos(\varphi - \psi) \\ X_2 = R_0 e^{(\varphi+\psi)} \sin(\varphi - \psi) \end{cases} \quad (15)$$

obtained by varying the parameters φ and ψ .¹ The constant R_0 is the radius of the inner circle and is assumed to be 50 mm. The outer radius delimiting the annular plate is $R_e = 260$ mm.

¹ The relationship between these parameters and the unit-speed parametrization can be explicitly evaluated as follows:

$$\varphi(S_1) = \ln \left| 1 + \frac{S_1}{\sqrt{2}R_0} \right|, \quad \psi(S_2) = \ln \left| 1 + \frac{S_2}{\sqrt{2}R_0} \right|. \quad (16)$$

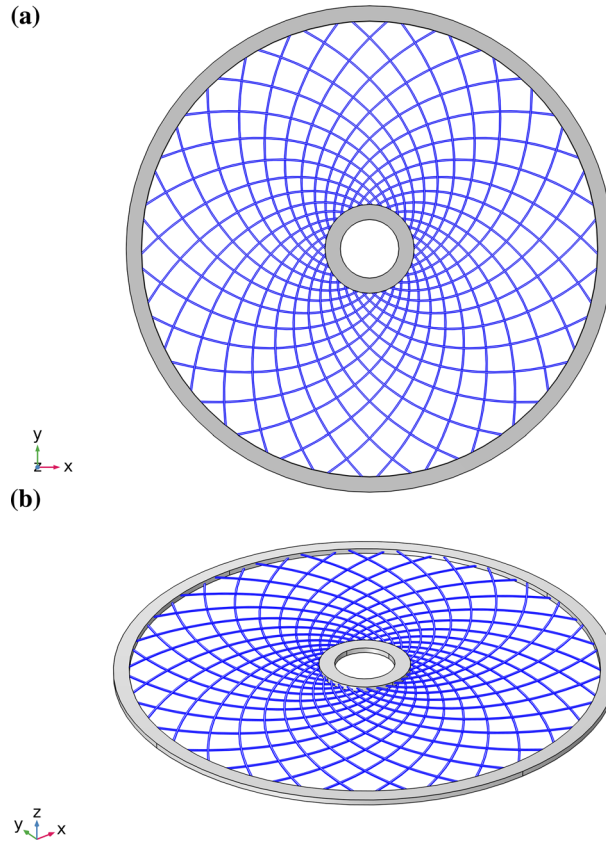


Fig. 2 A possible prototype that could be made with 3D printing: **a** top view; **b** perspective view

The stiffnesses characterizing the strain-gradient plate are computed with the expressions:

$$\begin{aligned}
 K_e &= \eta_e \frac{Y A}{p}, & K_s &= \eta_s \frac{G J_p}{h_p p^2}, & K_T &= \eta_T \frac{G J_t}{p}, \\
 K_g &= \eta_g \frac{Y J_{fg}}{p}, & K_n &= \eta_n \frac{Y J_{fn}}{p}
 \end{aligned} \tag{17}$$

where η_i are corrective coefficients and, moreover, A is the area of the fibers cross section, $J_t = 0.196 h^3 b$, $J_{fn} = h^3 b/12$, and $J_{fg} = b^3 h/12$ are the torsional, the normal bending, and the in-plane bending second moment of area of the fiber cross sections, respectively; in addition, $J_p = \pi r_p^4/2$ is the torsional second moment of area of the cylindrical pivot. Here, the two families of fibers are perfectly equal; therefore, it is not necessary to distinguish the stiffnesses belonging to different families. The variable p represents the pitch between two adjacent fibers. In particular, the pitch is determined by employing the three-dimensional sample shown in Fig. 2. This procedure has shown a linear dependence on the radial distance from the center of the annular plate that can be expressed with the relationship:

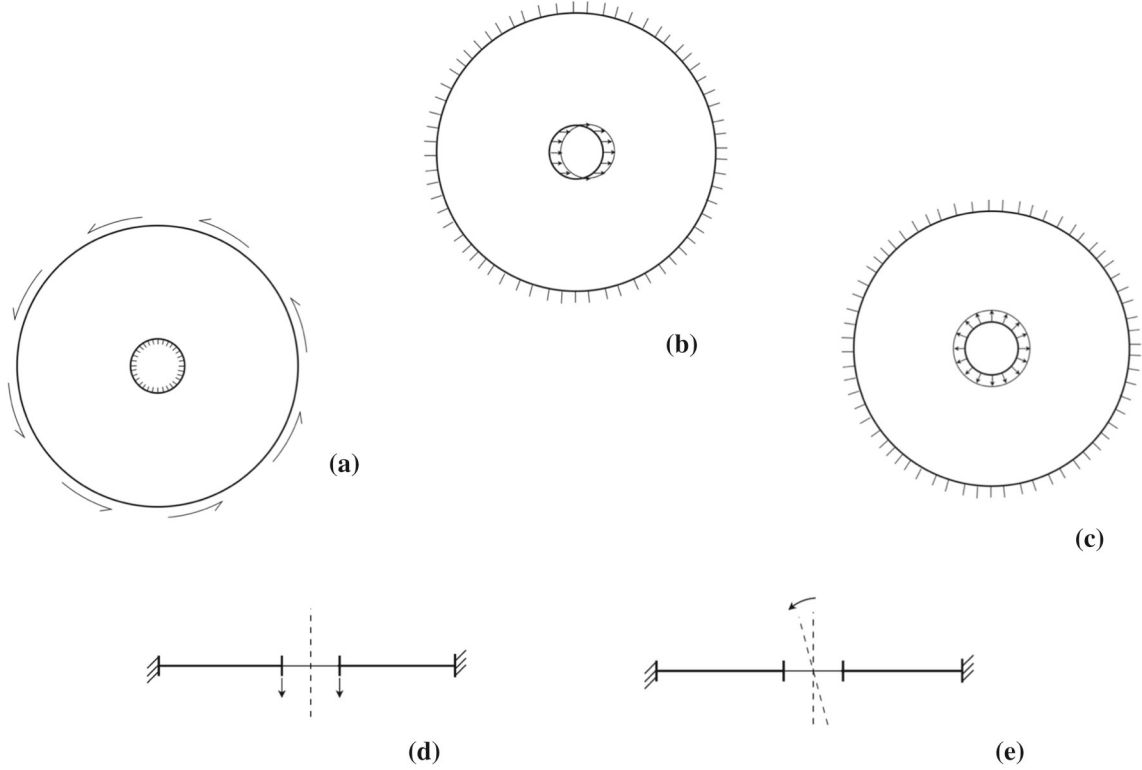
$$p = m \sqrt{2 (X_1^2 + X_2^2)} + q \tag{18}$$

where $q = -4 \times 10^{-2}$ mm and $m = 0.1085$.

The corrective coefficients η_i have been estimated by a micro-macro-identification as the one proposed in [47,48]. The obtained values are listed in Table 1. In this procedure, the material considered for the 3D model is homogeneous and isotropic and, thus, characterized by Young's modulus $Y = 1600$ MPa and Poisson's ratio $\nu = 0.4$.

Table 1 Tuned coefficients η

η_e	η_s	η_g	η_n	η_T
1.0	1.0	1.0	1.2	1.425

**Fig. 3** Schematic representation of the performed tests: **a** circumferential shear test; **b** radial shear test; **c** hole expansion test **d** pull-off test; **e** angular misalignment test

Moreover, the unit tangent vectors to the logarithmic spiral fibers are found to be

$$\mathbf{D}_1 \equiv \left(\frac{(X_1 - X_2)}{\sqrt{2(X_1^2 + X_2^2)}}, \frac{(X_1 + X_2)}{\sqrt{2(X_1^2 + X_2^2)}}, 0 \right), \quad \mathbf{D}_2 = \mathbf{D}_1 \times \mathbf{e}_3 \quad (19)$$

and their derivatives with respect to S_β are given by

$$\begin{aligned} \frac{d\mathbf{D}_1}{dS_1} &\equiv \left(\frac{-(X_1 + X_2)}{2(X_1^2 + X_2^2)}, \frac{(X_1 - X_2)}{2(X_1^2 + X_2^2)}, 0 \right), \\ \frac{d\mathbf{D}_2}{dS_2} &\equiv \left(\frac{-(X_1 - X_2)}{2(X_1^2 + X_2^2)}, \frac{-(X_1 + X_2)}{2(X_1^2 + X_2^2)}, 0 \right); \end{aligned} \quad (20)$$

consequently, the curvatures in the reference configuration become

$$\kappa_{g1}^0 = \kappa_{g2}^0 = -\frac{1}{\sqrt{2(X_1^2 + X_2^2)}} \quad (21)$$

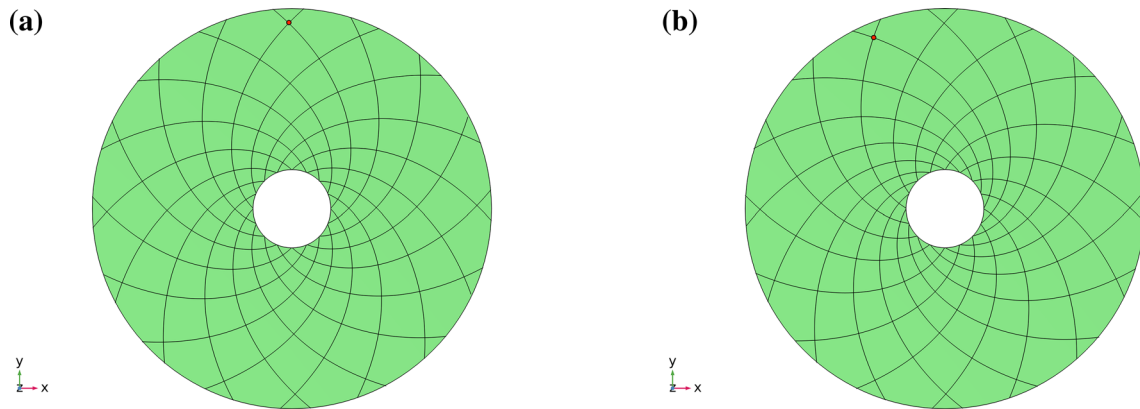


Fig. 4 Circumferential shear test: **a** Reference configuration; **b** Current configuration at the maximum angle attained of 23 degrees. Black solid lines represent material lines following some paths of logarithmic spirals. The same material point is highlighted in red in the two configurations for better understanding of the setup

3 Numerical simulations and discussion

This section is devoted to numerically investigating the mechanical behavior of a 2D material made of an orthogonal net of curved fibers arranged following equiangular logarithmic spirals. To this end, several significant tests are performed on an annular plate showing the nonlinear responses when large displacements are applied to the boundaries. The employed model, sketched in the previous section, is programmed into a finite element software, namely COMSOL Multiphysics, directly through its weak formulation deduced from the elastic energy (14). For technical details related to the implementation, the reader can refer to the works [36,49,50], while for possible improvements, see [51–54].

Specifically, tests that are conceived to illustrate the peculiar responses of the considered bidimensional elastic material are (see Fig. 3):

1. Circumferential shear test;
2. Radial shear test;
3. Hole expansion test;
4. Pull-off test;
5. Angular misalignment test.

Only kinematic essential boundary conditions have been implemented in all the performed tests because of their simplicity. Since the model employed is a second-gradient one, proper boundary conditions involve assigning the displacement and its gradient.

In the first simulation, a *circumferential shear test* is carried out. Here, we fix the inner circle and rotate the outer one at an increasing angle. The simulation is stopped at the angle of 23 degrees because, after this threshold, an out-of-plane buckling occurs. Regarding the boundary condition related to the displacement gradient, the in-plane normal derivative of the out-of-plane displacement component is set to zero to describe a clamping condition. In detail,

$$\nabla_x u_3 \cdot \boldsymbol{\nu} = 0 \quad (22)$$

where $\boldsymbol{\nu}$ is planar unit normal to the boundaries.

Figure 4 shows the annular plate prior the deformation and the equilibrium shape for the maximum angle imposed, namely 23 degrees. To facilitate the characterization of the deformed configuration, we put a red spot fixed on the plate. In Figs. 5, 6, and 7, the significant measures of deformation are displayed. In this case, one family of fibers is stretched, and the other is compressed, especially in the central zone close to the inner circle; the shear distortion angle is almost negligible; the change of geodesic curvature localizes near the boundary circles as it could be expected.

Figure 8 exhibits the characteristic diagram of the reaction torque versus the applied angle to the outer circle. In the examined range, the behavior is predominantly linear. This plot has been evaluated using Castigliano's theorem by numerically differentiating the elastic energy with respect to the imposed angle.

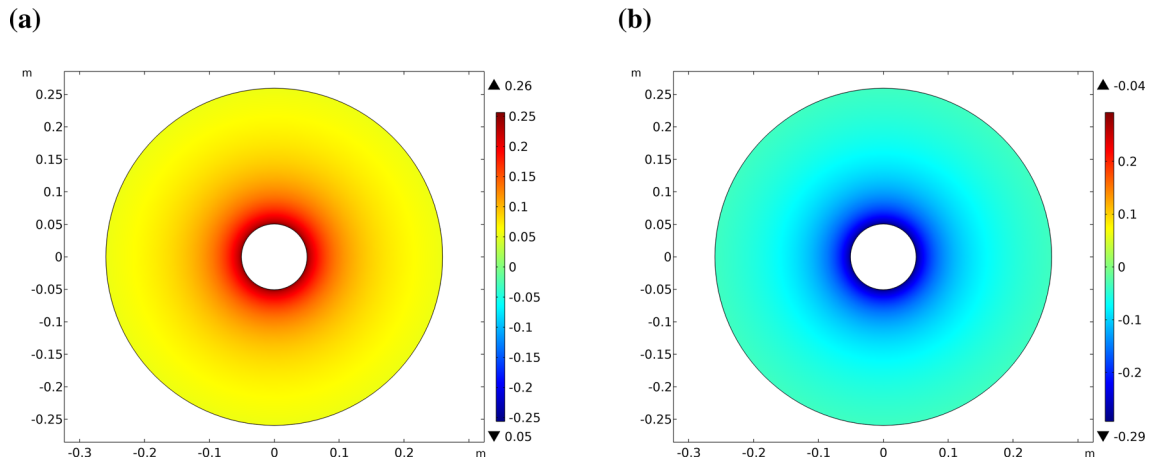


Fig. 5 Circumferential shear test: elongation **a** ϵ_1 ; **b** ϵ_2

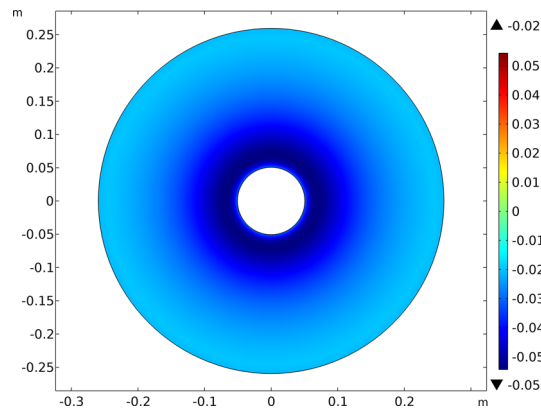


Fig. 6 Circumferential shear test: shear distortion angle γ

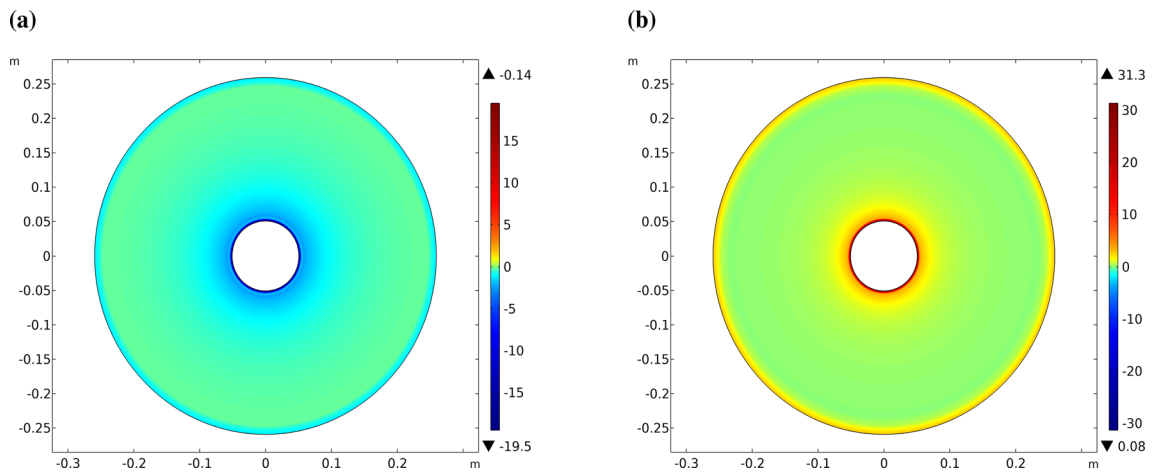


Fig. 7 Circumferential shear test: geodesic curvature change **a** $\Delta\kappa_{g1}$; **b** $\Delta\kappa_{g2}$

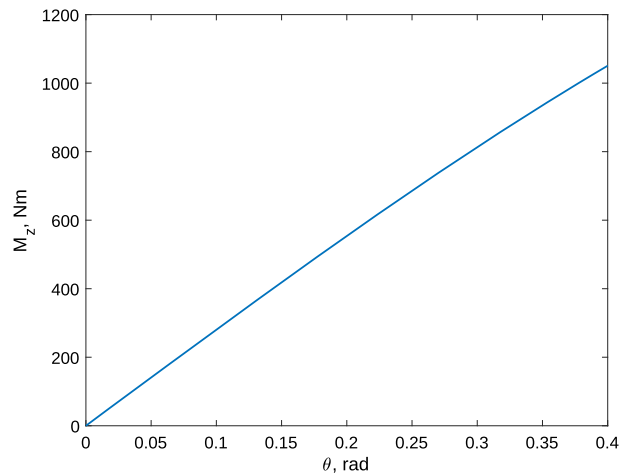


Fig. 8 Circumferential shear test: torque vs angle

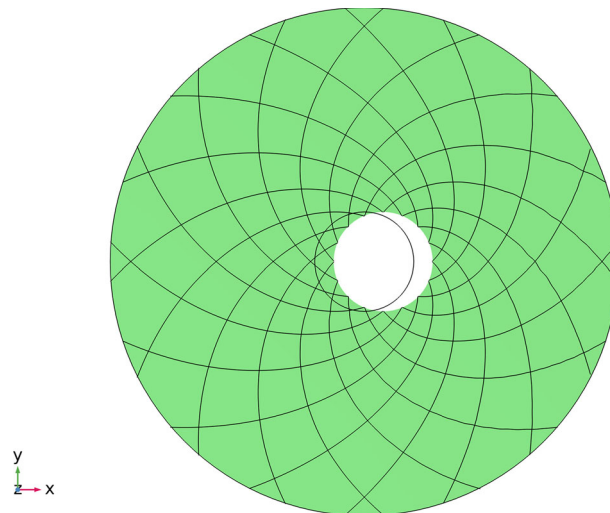


Fig. 9 Radial shear test: Current configuration after a radial displacement of $0.386R_0$

In the second test, we clamp the outer circle and rigidly translate the inner one radially, keeping the condition (22) also for this boundary. The outcome of this *radial shear test* is shown in Fig. 9, where the current equilibrium shape is reported alongside the inner circle with a solid black line in the reference position for a displacement of $0.386R_0$.

The deformation measures related to this test are plotted in Figs. 10, 11, and 12. Here, both families of fibers are subject simultaneously to stretch and compression, having a mirror symmetry pattern. The shear distortion angle is more significant than in the previous case reaching the value of about 10 degrees. The change of geodesic curvature is also localized nearby the boundaries but with a more complex distribution.

Figure 13 depicts the force versus displacement plot that characterizes this radial shear test. Notwithstanding the relatively large enforced displacement, the whole behavior of the annular plate is still linear.

In this case, if a small amount of pressure normal to the plane of the annular plate is applied, a buckled shape occurs after a critical value of the radial displacement ($R_0/5$), as shown in Fig. 14a. The pattern of this shape is characterized by a prominent bulge in the compressed zone, while the left region affected by overall stretching presents several wrinkling. To confirm this complex shape, a numerical simulation has been performed with a more detailed and time-consuming 3D finite element model using the Saint Venant–Kirchhoff constitutive behavior for hyperelastic materials in nonlinear regime with an accurate description of the geometry of the fibers. Figure 14b reproduces the plot of the buckled shape with the 3D model. Comparing

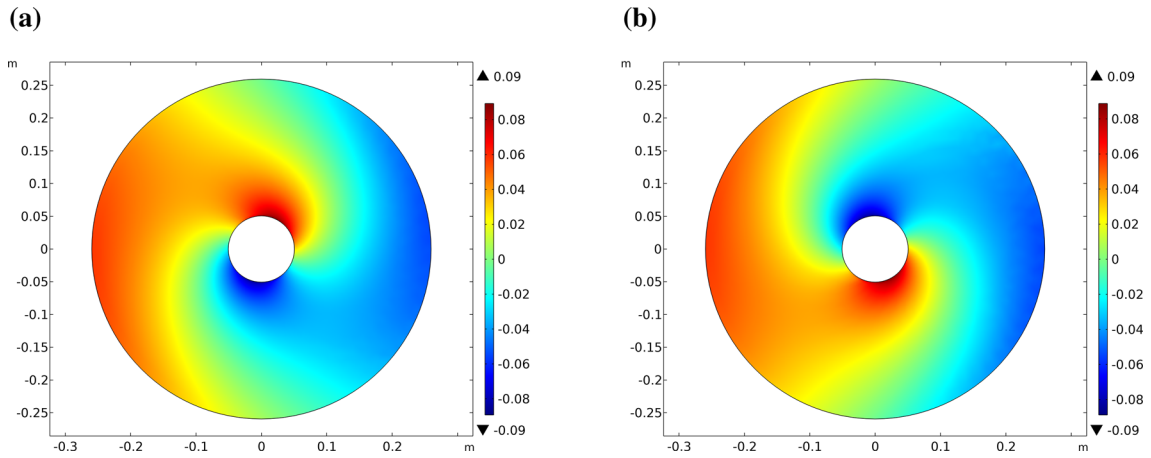


Fig. 10 Radial shear test: elongation **a** ε_1 ; **b** ε_2

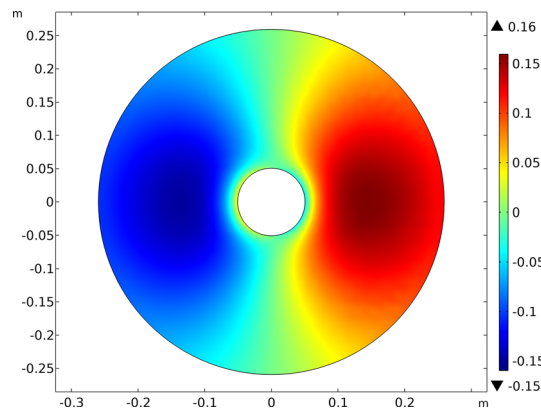


Fig. 11 Radial shear test: shear distortion angle γ

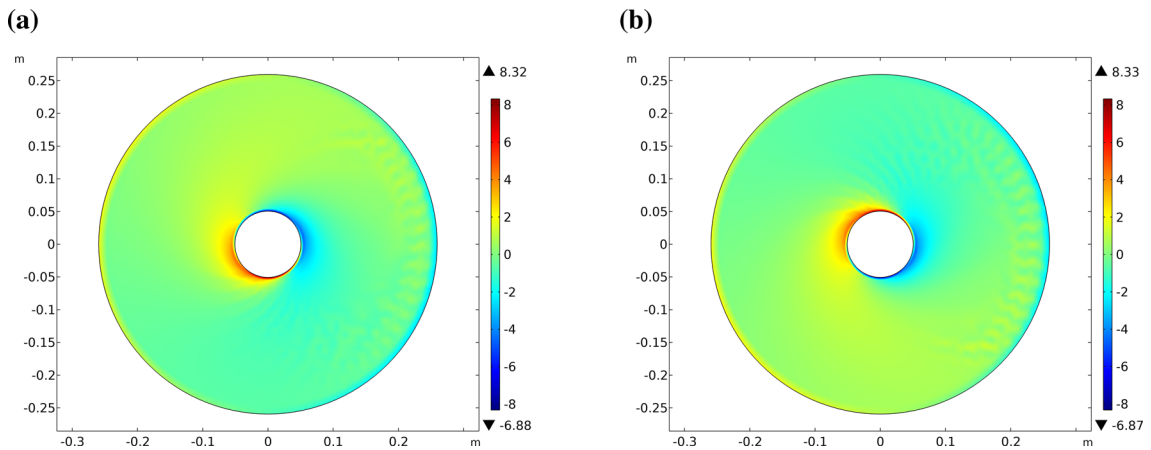


Fig. 12 Radial shear test: geodesic curvature change **a** $\Delta\kappa_{g1}$; **b** $\Delta\kappa_{g2}$

the results obtained by the two formulations, namely the 2D and 3D ones, shows a good agreement between the models corroborating the validity of the simplified bidimensional second-gradient plate theory adopted.

In the third case, we analyze a *hole expansion test*, where the inner circle is radially and isotropically expanded, holding the clamp condition of Eq. (22) on both boundaries (see, Fig. 15, for the current configuration at maximum imposed displacement).

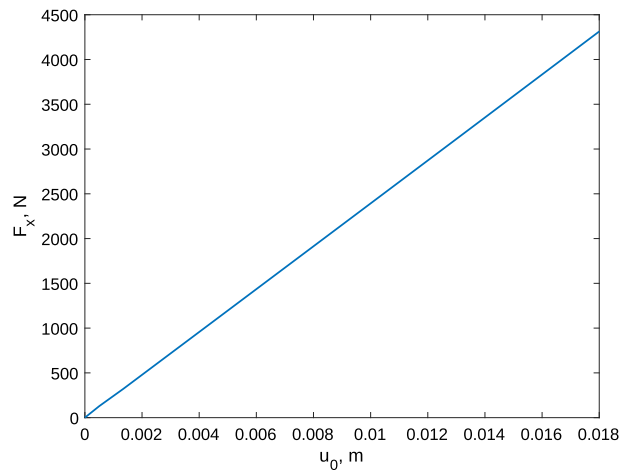


Fig. 13 Radial shear test: radial force vs imposed displacement

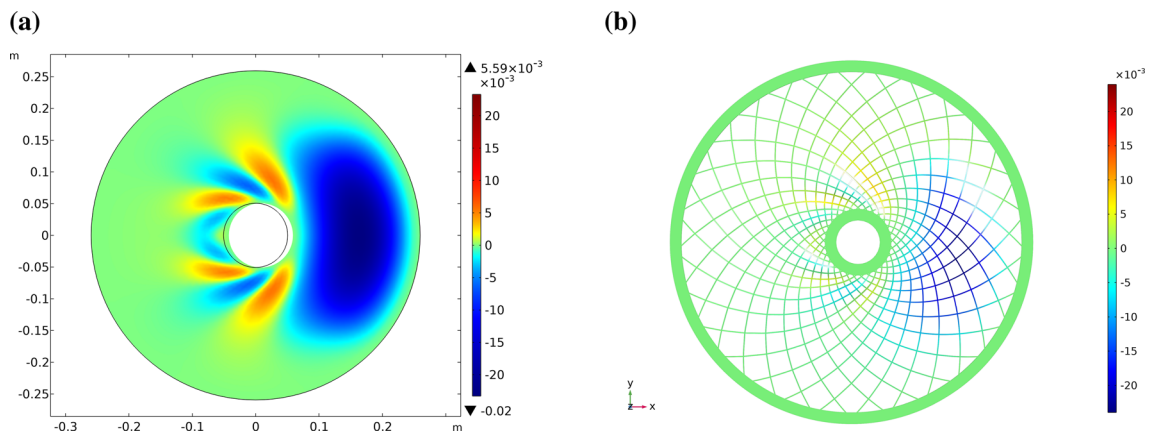


Fig. 14 Buckling occurring during the radial shear test: **a** 2D model; **b** 3D model

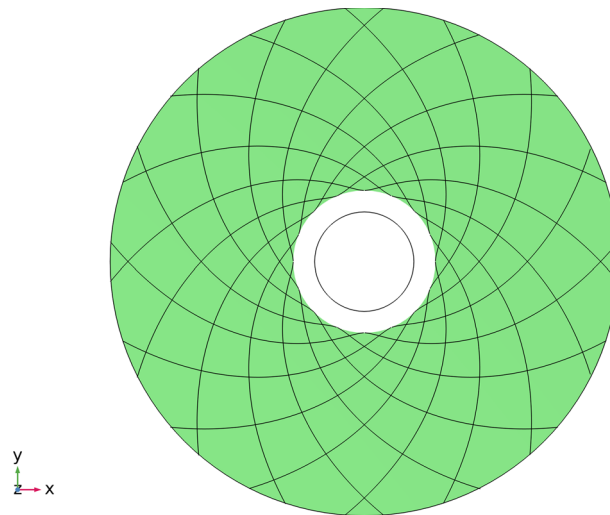


Fig. 15 Hole expansion test: current configuration for the maximal radial displacement of $0.44 R_0$

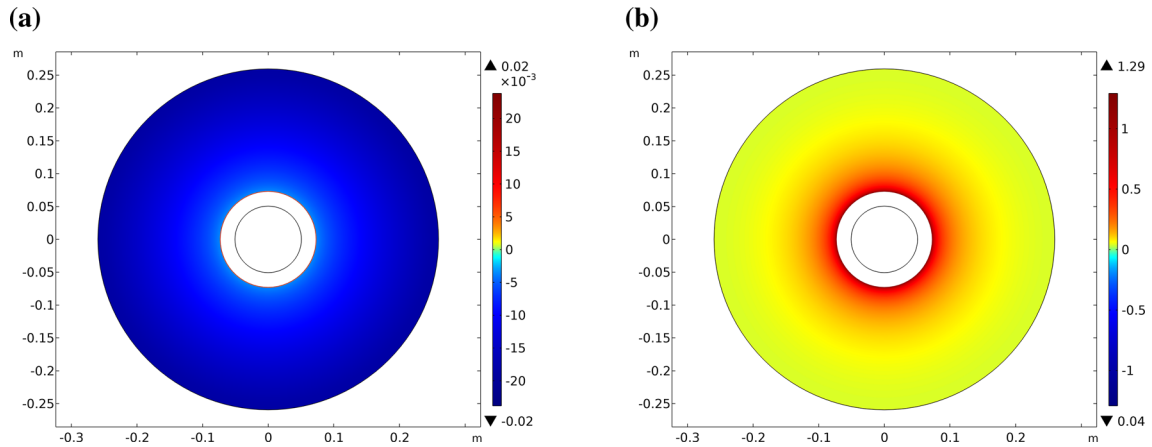


Fig. 16 Hole expansion test: **a** elongation ε_β ; **b** shear distortion angle γ

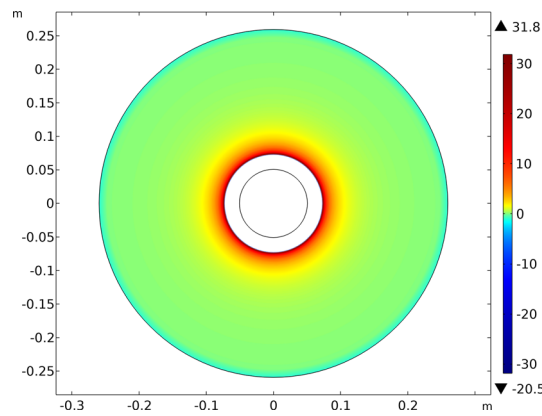


Fig. 17 Hole expansion test: geodesic curvature change $\Delta\kappa_{g\beta}$

The significant measures of deformation for this case are plotted in Figs. 16 and 17. Due to the symmetry of the applied displacement, the deformation is also symmetric. Therefore, the elongations, which are negative, of the two fiber families are the same, as well as the change in the geodesic curvature. Let us remark that the compression is almost linearly distributed over the entire annular plate having the maximum located in the correspondence of the outer circle. Only a very narrow boundary layer of stretched fiber is localized on the inner circle. On the contrary, the distribution of the shear distortion angle tends to localize around the inner ring and becomes flat, approaching the outer boundary. As regards the change in the geodesic curvature, the most prominent deformation is localized near the inner circle and is zero almost everywhere except the boundaries.

Figure 18 displays the inner radial pressure versus the radial applied displacement. In this case, an appreciable nonlinear behavior is present.

Subsequently, a *pull-off test* is performed on the annular plate. The outer circle is fixed, while the inner circle is rigidly translated in the out-of-plane direction until a displacement of $2R_0$ is reached. As the two boundary circles always remain parallel during the test starting from the reference configuration, the clamp conditions are once again given by Eq. (22). Figure 19 shows the current configuration for the maximum displacement.

In this new case, the set of deformation measures is richer than in the previous instances since the out-of-plane curvature and the torsion of fibers become different from zero. Figures 20, 21, and 22 illustrate all of them. The elongations, which are positive for all the fibers, have a linear distribution depending on the radius with the maximum value at the outer circle as shown in Fig. 20a. The shear distortion angle is also almost linear in the body of the annular plate with the maximum value near the inner circle but with more evident deviations close to the boundaries. The shear distortion angle also has almost a linear distribution in the body of the annular plate; on the contrary, the maximum value is near the inner circle, and more evident deviations can be noticed close to the boundaries (see Fig. 20b).

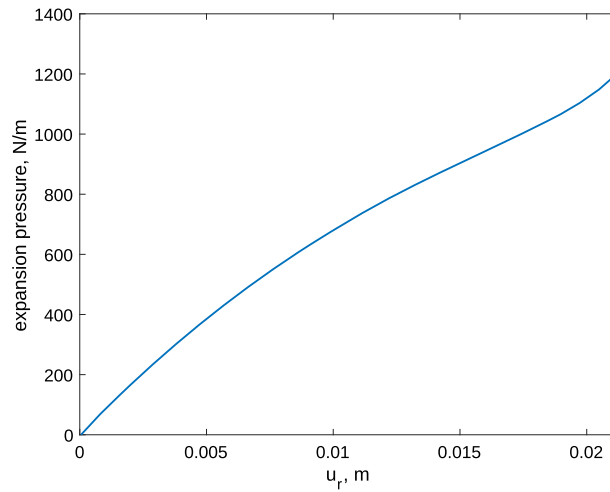


Fig. 18 Hole expansion test: inner radial pressure vs displacement

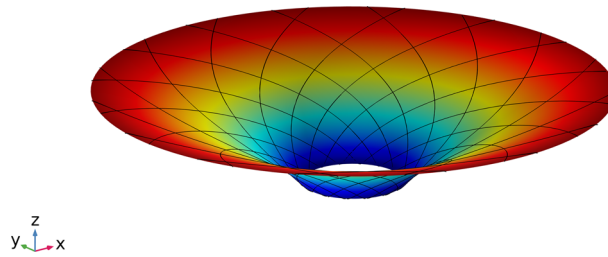


Fig. 19 Pull-off test: Current configuration for an out-of-plane displacement of the inner ring equal to $2R_0$

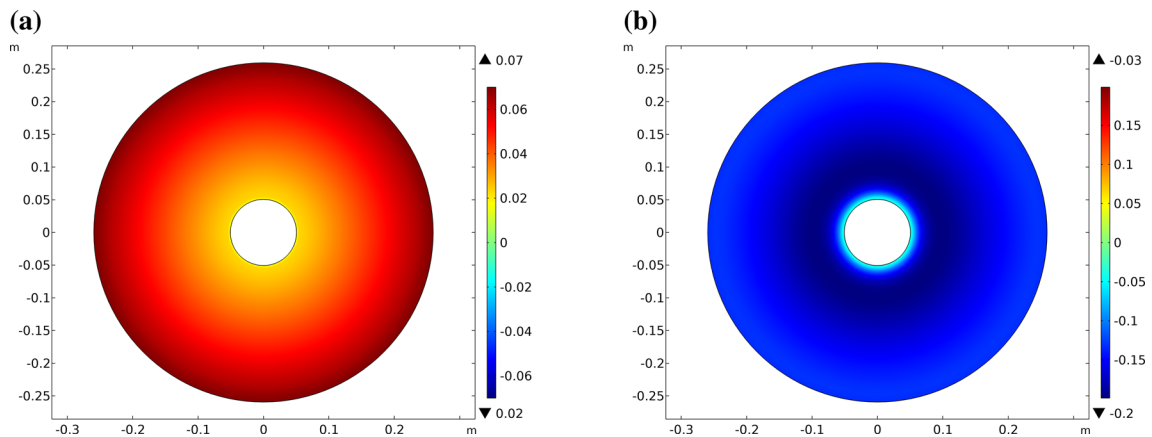


Fig. 20 Pull-off test: **a** elongation ε_β ; **b** shear distortion angle γ

All the deformation measures related to the second-gradient contribution, namely the curvatures and the torsions, are almost negligible in the body of the annular plate but become significant in boundary layers nearby the two circles that define the considered elastic surface as apparent from Figs. 21 and 22.

Figure 23 shows the resultant out-of-plane component of the reaction force versus the applied displacement in the same direction. In this case, the nonlinear behavior is predominant, entailing a feeble resistance for small displacements that quickly grows as the displacement increases.

Finally, an *angular misalignment test* is performed on the annular plate imposing a relative rotation until $\pi/2$ of the two out-of-plane normal axes of the boundary circles. Specifically, the outer ring is fixed, while the inner one is rotated at an increasing angle with respect to a radial axis lying on the plane of the plate. The clamp condition is the same Eq. (22) for the outer circle. The inner ring has been subject to a different treatment

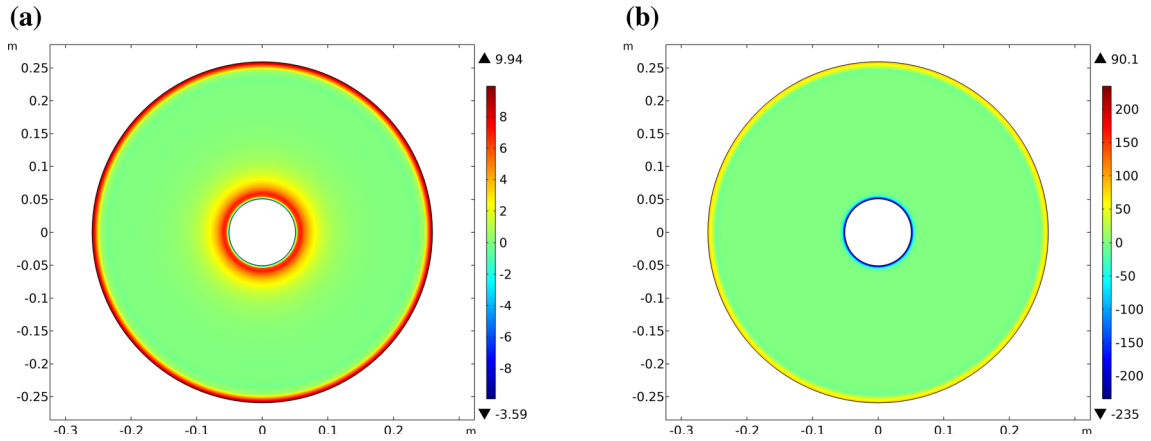


Fig. 21 Pull-off test: curvature change **a** geodesic $\Delta\kappa_{g\beta}$; **b** out-of-plane $\kappa_{n\beta}$

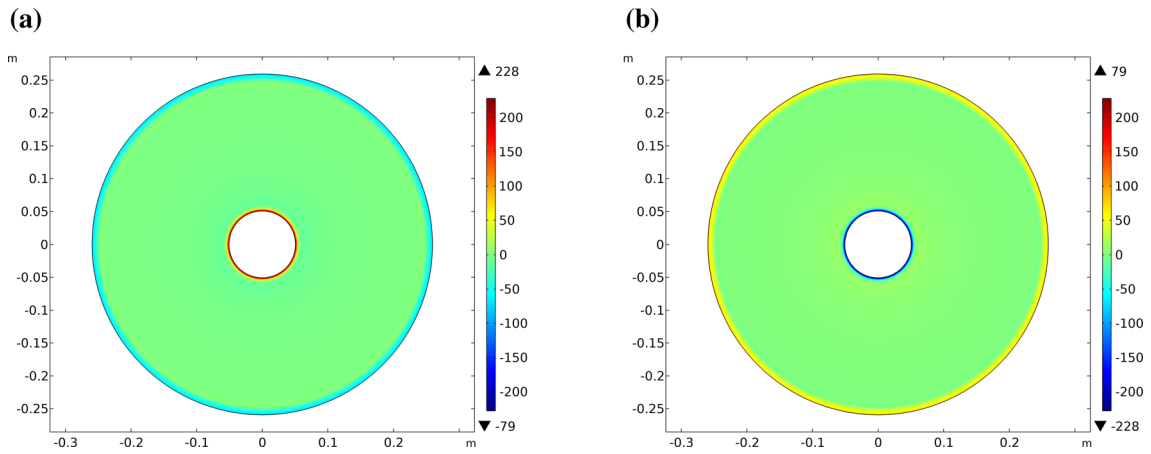


Fig. 22 Pull-off test: twisting change **a** κ_{T1} ; **b** κ_{T2}

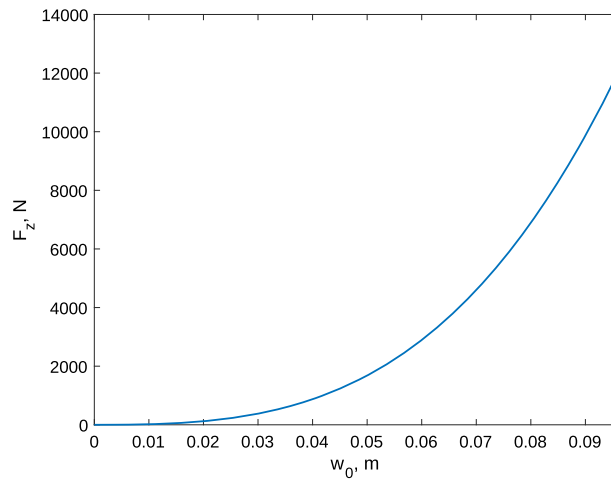


Fig. 23 Pull-off test: out-of-plane force vs imposed displacement

instead. Since the condition ensuring the clamp is much more complicated from a mathematical point of view due to the large rotation of the ring, the same condition has been obtained equivalently, as explained in the following. A narrow annular ring is added in correspondence with the hole, and the desired rigid rotation is imposed to this additional part (see Fig. 24). This simple trick clearly sets an equivalent differential condition

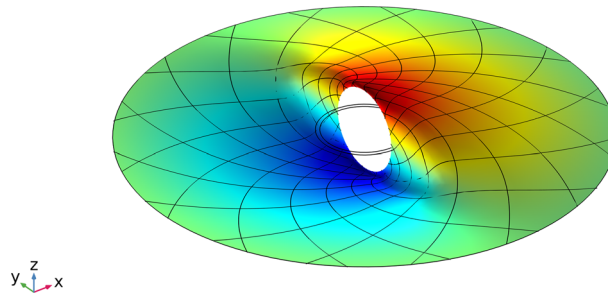


Fig. 24 Angular misalignment test: current configuration for a rotation of the inner ring of angle of $\pi/2$

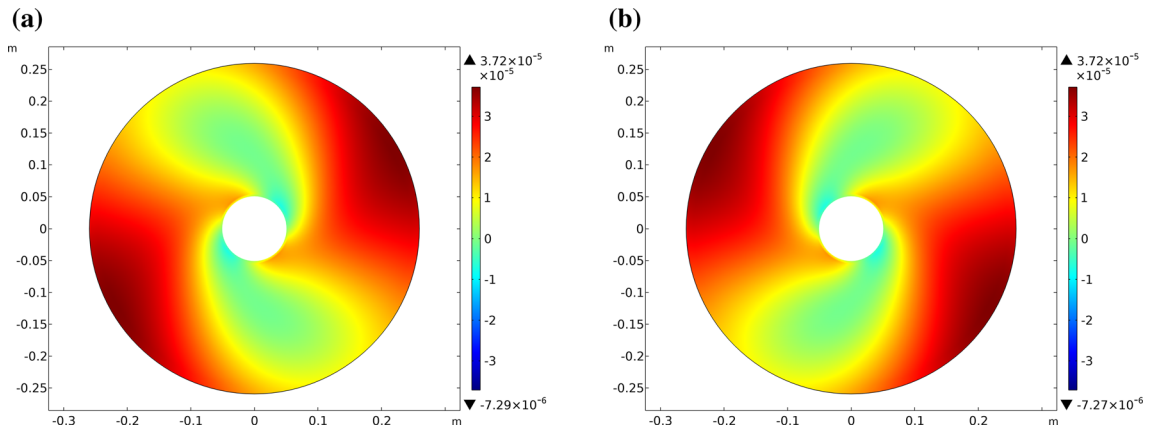


Fig. 25 Angular misalignment test: elongation **a** ε_1 ; **b** ε_2

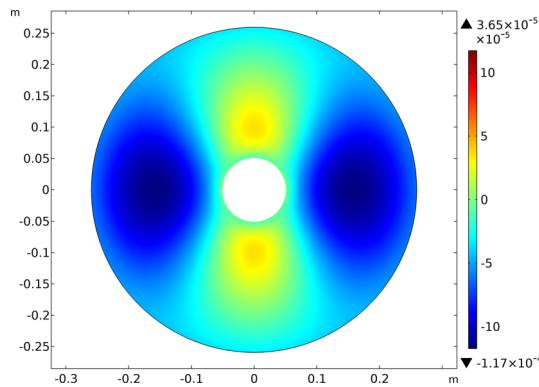


Fig. 26 Angular misalignment test: shear distortion angle γ

for the clamp inside the annular plate forcing the tangent plane to the surface to be parallel to the plane of the inner circle.

Figures 25, 26, and 27 display the deformation measures characteristic of the tangent behavior to the elastic surface, namely the fiber elongations, the shear distortion angle, and the geodesic curvature changes of the fibers. In this case, these deformation measures have small amplitudes and hence are less significant, especially for what concerns the shear distortion angle and the geodesic curvature change because of the smaller values of the related stiffnesses.

Figures 28 and 29 exhibit the deformation measures related to the out-of-plane behavior, i.e., the out-of-plane curvature change and the twisting change of the fibers. The out-of-plane measures of deformations, as expected, have more pronounced amplitudes in this case representing an essential part of the overall deformation.

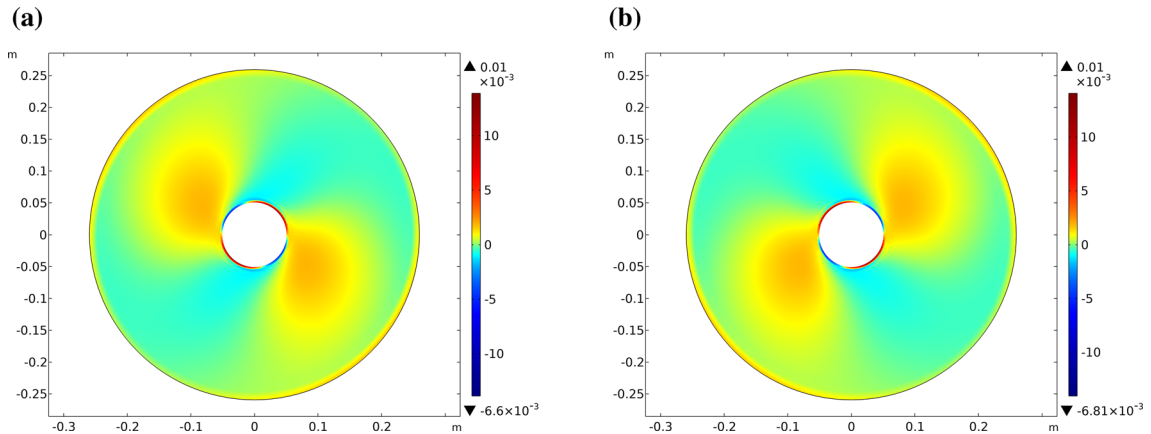


Fig. 27 Angular misalignment test: geodesic curvature change **a** $\Delta\kappa_{g1}$; **b** $\Delta\kappa_{g2}$

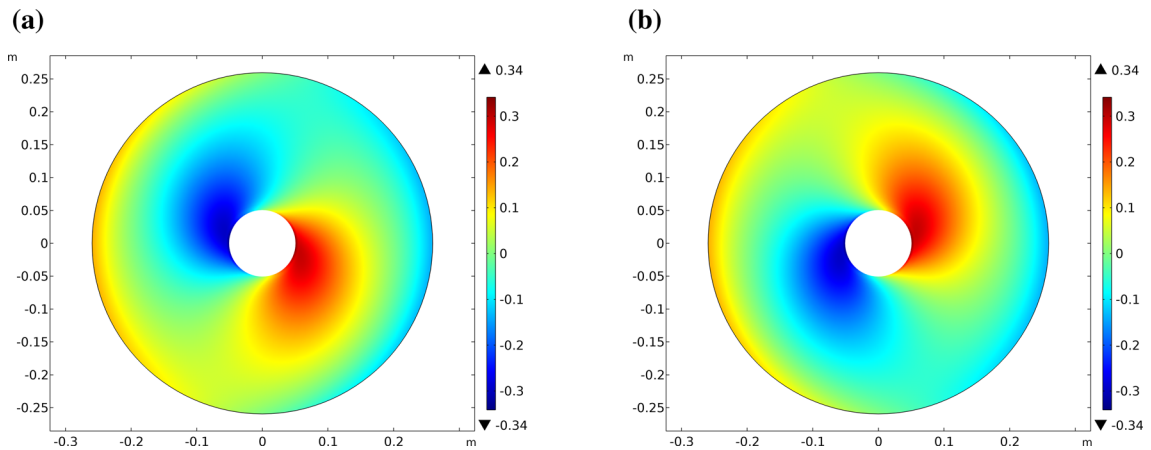


Fig. 28 Angular misalignment test: out-of-plane curvature change **a** κ_{n1} ; **b** κ_{n2}

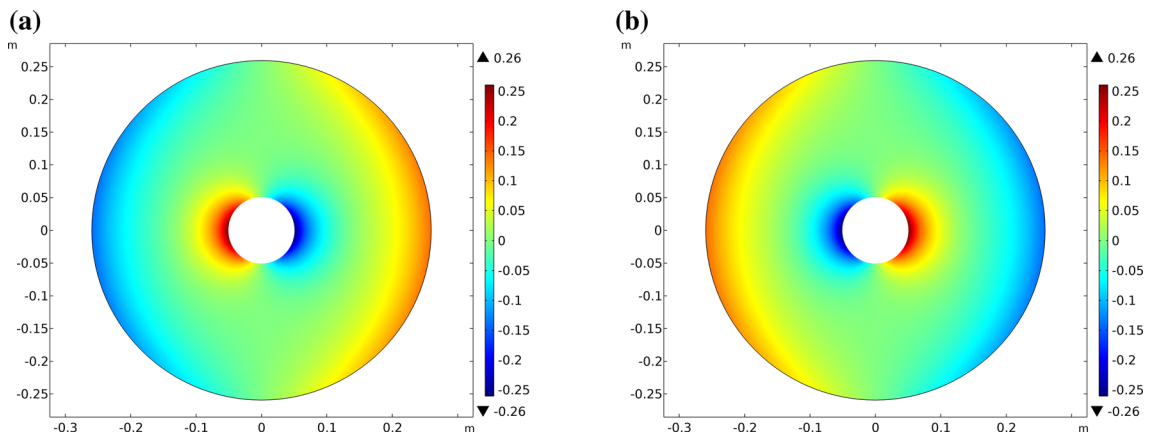


Fig. 29 Angular misalignment test: twisting change **a** κ_{T1} ; **b** κ_{T2}

Figure 30 reports the resultant reaction torque versus the applied angle. Analogously to the previous case, the nonlinear behavior is significant, showing a very weak resistance for small angles that quickly raises as the angle increases.

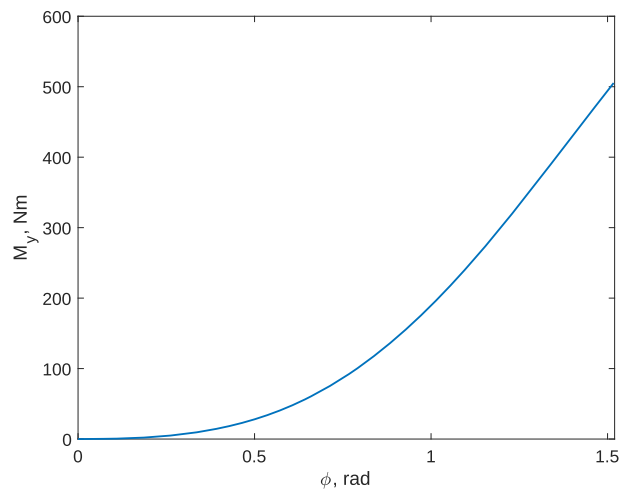


Fig. 30 Angular misalignment test: reaction torque vs imposed angle

4 Conclusions

In this paper, we have numerically studied the behaviors of an archetypal prototype, namely an annular plate with fibers arranged according to logarithmic spirals following the framework proposed by David J. Steigmann [33,55,56] for describing a system made by an orthogonal net of fibers. The model falls in the category of continuum elastic surfaces of higher-order gradients [57–59]. This formulation is reasonably comprehensive since it is able to treat several mechanisms of deformations, including the bending and twisting of the fibers. Moreover, it has been proven in many experimental tests that the model is actually accurate and predictive [60–64].

The numerical tests show the nonlinear character of the system as well as its strength within the elastic regime, making it suitable for many technical applications such as separating septum with some shield capabilities, reinforcement for membranes in a valve, and flexible joints.

A final word for the future directions of this research is noteworthy. In this paper, we have only analyzed the elastic behavior in a static regime, although nonlinear. For a complete assessment of the full potential of the system under study, a thorough examination related to its dynamic properties [65–73] and inelastic behavior, i.e., in case of plasticity and damage [46,74–82], is also compelling.

Open Access This article is licensed under a Creative Commons Attribution 4.0 International License, which permits use, sharing, adaptation, distribution and reproduction in any medium or format, as long as you give appropriate credit to the original author(s) and the source, provide a link to the Creative Commons licence, and indicate if changes were made. The images or other third party material in this article are included in the article's Creative Commons licence, unless indicated otherwise in a credit line to the material. If material is not included in the article's Creative Commons licence and your intended use is not permitted by statutory regulation or exceeds the permitted use, you will need to obtain permission directly from the copyright holder. To view a copy of this licence, visit <http://creativecommons.org/licenses/by/4.0/>.

Funding Open access funding provided by Università degli Studi dell'Aquila within the CRUI-CARE Agreement.

Declarations

Conflict of interest: The authors declare that they have no conflict of interest.

References

1. Michell, A.G.M.: LVIII. The limits of economy of material in frame-structures. London, Edinburgh, and Dublin Philos. Magaz. J. Sci. **8**(47), 589–597 (1904)
2. Techebychev, P.L.: Sur la coupe des vêtements. In: Association Française Pour L'avancement des Sciences, Congrès de Paris, pp. 154–155 (1878)
3. Aydin, G., Yildizdag, M.E., Abali, B.E.: Strain-gradient modeling and computation of 3-D printed metamaterials for verifying constitutive parameters determined by asymptotic homogenization. In: Giorgio, I., Placidi, L., Barchiesi, E., Abali, B.E.,

- Altenbach, H. (eds.) *Theoretical Analyses, Computations, and Experiments of Multiscale Materials*. Advanced Structured Materials, vol. 175, pp. 343–357. Springer, Cham (2022)
4. Schneevoigt, H., Stelzner, K., Yilmaz, B., Abali, B.E., Klunker, A., Völlmecke, C.: Sustainability in additive manufacturing: exploring the mechanical potential of recycled PET filaments. *Composit. Adv. Mater.* **30**, 26349833211000064 (2021)
 5. Özen, A., Ganzosch, G., Barchiesi, E., Auhl, D.W., Müller, W.H.: Investigation of deformation behavior of PETG-FDM-printed metamaterials with pantographic substructures based on different slicing strategies. *Composit. Adv. Mater.* **30**, 26349833211016476 (2021)
 6. Harsch, J., Ganzosch, G., Barchiesi, E., Ciallella, A., Eugster, S.R.: Experimental analysis, discrete modeling and parameter optimization of SLS-printed bi-pantographic structures. *Math. Mech. Solids*, 10812865221107623 (2022)
 7. Abali, B.E., Barchiesi, E.: Additive manufacturing introduced substructure and computational determination of metamaterials parameters by means of the asymptotic homogenization. *Continuum Mech. Thermodyn.* **33**(4), 993–1009 (2021)
 8. Desmorat, B., Spagnuolo, M., Turco, E.: Stiffness optimization in nonlinear pantographic structures. *Math. Mech. Solids* **25**(12), 2252–2262 (2020)
 9. Stilz, M., Plappert, D., Gutmann, F., Hiermaier, S.: A 3D extension of pantographic geometries to obtain metamaterial with semi-auxetic properties. *Math. Mech. Solids* **27**(4), 673–686 (2022)
 10. Lai, M., Eugster, S.R., Reccia, E., Spagnuolo, M., Cazzani, A.: Corrugated shells: an algorithm for generating double-curvature geometric surfaces for structural analysis. *Thin-Walled Struct.* **173**, 109019 (2022)
 11. Wang, X., Zhang, L., Song, B., Zhang, Z., Zhang, J., Fan, J., Wei, S., Han, Q., Shi, Y.: Tunable mechanical performance of additively manufactured plate lattice metamaterials with half-open-cell topology. *Compos. Struct.* **300**, 116172 (2022)
 12. Prager, W.: Optimal layout of cantilever trusses. *J. Optim. Theory Appl.* **23**(1), 111–117 (1977)
 13. Alibert, J.-J., Seppecher, P., dell’Isola, F.: Truss modular beams with deformation energy depending on higher displacement gradients. *Math. Mech. Solids* **8**(1), 51–73 (2003)
 14. dell’Isola, F., Andreaus, U., Placidi, L.: At the origins and in the vanguard of peridynamics, non-local and higher-gradient continuum mechanics: an underestimated and still topical contribution of Gabrio Piola. *Math. Mech. Solids* **20**(8), 887–928 (2015)
 15. Turco, E., dell’Isola, F., Cazzani, A., Rizzi, N.L.: Hencky-type discrete model for pantographic structures: numerical comparison with second gradient continuum models. *Zeitschrift für angewandte Mathematik und Physik* **67**(4), 85 (2016)
 16. Barchiesi, E., Eugster, S.R., Placidi, L., dell’Isola, F.: Pantographic beam: a complete second gradient 1D-continuum in plane. *Zeitschrift für angewandte Mathematik und Physik* **70**(5), 135 (2019)
 17. Abdoul-Anziz, H., Seppecher, P., Bellis, C.: Homogenization of frame lattices leading to second gradient models coupling classical strain and strain-gradient terms. *Math. Mech. Solids* **24**(12), 3976–3999 (2019)
 18. Abdoul-Anziz, H., Seppecher, P.: Strain gradient and generalized continua obtained by homogenizing frame lattices. *Math. Mech. Complex Syst.* **6**(3), 213–250 (2018)
 19. Eugster, S.R., dell’Isola, F., Fedele, R., Seppecher, P.: Piola transformations in second-gradient continua. *Mech. Res. Commun.* **120**, 103836 (2022)
 20. dell’Isola, F., Eugster, S.R., Fedele, R., Seppecher, P.: Second-gradient continua: from Lagrangian to Eulerian and back. *Math. Mech. Solids*, 10812865221078822 (2022)
 21. Eremeyev, V.A.: On the material symmetry group for micromorphic media with applications to granular materials. *Mech. Res. Commun.* **94**, 8–12 (2018)
 22. Misra, A., Poorsolhjouy, P.: Grain-and macro-scale kinematics for granular micromechanics based small deformation micromorphic continuum model. *Mech. Res. Commun.* **81**, 1–6 (2017)
 23. Schulte, J., Dittmann, M., Eugster, S.R., Hesch, S., Reinicke, T., dell’Isola, F., Hesch, C.: Isogeometric analysis of fiber reinforced composites using Kirchhoff-Love shell elements. *Comput. Methods Appl. Mech. Eng.* **362**, 112845 (2020)
 24. Turco, E., Barchiesi, E., dell’Isola, F.: In-plane dynamic buckling of duoskelion beam-like structures: discrete modeling and numerical results. *Math. Mech. Solids* **27**(7), 1164–1184 (2022)
 25. Misra, A., Placidi, L., dell’Isola, F., Barchiesi, E.: Identification of a geometrically nonlinear micromorphic continuum via granular micromechanics. *Zeitschrift für angewandte Mathematik und Physik* **72**(4), 1–21 (2021)
 26. Solyaev, Y., Lurie, S., Barchiesi, E., Placidi, L.: On the dependence of standard and gradient elastic material constants on a field of defects. *Math. Mech. Solids* **25**(1), 35–45 (2020)
 27. La Valle, G., Massoumi, S.: A new deformation measure for micropolar plates subjected to in-plane loads. *Continuum Mech. Thermodyn.* **34**(1), 243–257 (2022)
 28. La Valle, G.: A new deformation measure for the nonlinear micropolar continuum. *Z. Angew. Math. Phys.* **73**(2), 1–26 (2022)
 29. Altenbach, J., Altenbach, H., Eremeyev, V.A.: On generalized Cosserat-type theories of plates and shells: a short review and bibliography. *Arch. Appl. Mech.* **80**(1), 73–92 (2010)
 30. Eremeyev, V.A., Pietraszkiewicz, W.: Material symmetry group of the non-linear polar-elastic continuum. *Int. J. Solids Struct.* **49**(14), 1993–2005 (2012)
 31. Eremeyev, V.A., Pietraszkiewicz, W.: Material symmetry group and constitutive equations of micropolar anisotropic elastic solids. *Math. Mech. Solids* **21**(2), 210–221 (2016)
 32. Dos Reis, F., Ganghoffer, J.F.: Construction of micropolar continua from the asymptotic homogenization of beam lattices. *Comput. Struct.* **112**, 354–363 (2012)
 33. Steigmann, D.J., dell’Isola, F.: Mechanical response of fabric sheets to three-dimensional bending, twisting, and stretching. *Acta Mechanica Sinica* **31**(3), 373–382 (2015)
 34. Giorgio, I., Rizzi, N.L., Turco, E.: Continuum modelling of pantographic sheets for out-of-plane bifurcation and vibrational analysis. *Proceed. Royal Soc. A: Math. Phys. Eng. Sci.* **473**(2207), 20170636 (2017)
 35. Shirani, M., Luo, C., Steigmann, D.J.: Cosserat elasticity of lattice shells with kinematically independent flexure and twist. *Continuum Mech. Thermodyn.* **31**(4), 1087–1097 (2019)
 36. Giorgio, I., Ciallella, A., Scerrato, D.: A study about the impact of the topological arrangement of fibers on fiber-reinforced composites: some guidelines aiming at the development of new ultra-stiff and ultra-soft metamaterials. *Int. J. Solids Struct.* **203**, 73–83 (2020)

37. Giorgio, I.: Lattice shells composed of two families of curved Kirchhoff rods: an archetypal example, topology optimization of a cycloidal metamaterial. *Continuum Mech. Thermodyn.* **33**(4), 1063–1082 (2021)
38. Eremeyev, V.A., dell’Isola, F., Boutin, C., Steigmann, D.: Linear pantographic sheets: existence and uniqueness of weak solutions. *J. Elastic.* **132**(2), 175–196 (2018)
39. Jamun Kumar, N., Dhas, B., Srinivasa, A.R., Reddy, J.N., Roy, D.: A novel four-field mixed FE approximation for Kirchhoff rods using Cartan’s moving frames. *Comput. Methods in Appl. Mech. Eng.*, 115094 (2022)
40. Harsch, J., Capobianco, G., Eugster, S.R.: Finite element formulations for constrained spatial nonlinear beam theories. *Math. Mech. Solids* **26**(12), 1838–1863 (2021)
41. Turco, E.: Modeling of three-dimensional beam nonlinear vibrations generalizing Hencky’s ideas. *Math. Mech. Solids*, 10812865211067987 (2022)
42. Greco, L.: An iso-parametric G^1 -conforming finite element for the nonlinear analysis of Kirchhoff rod. Part I: the 2D case. *Continuum Mech. Thermodynam.*, 1–24 (2020)
43. Greco, L., Cuomo, M., Castello, D., Scrofani, A.: An updated lagrangian Bézier finite element formulation for the analysis of slender beams. *Math. Mech. Solids*, 10812865221101549 (2022)
44. Spagnuolo, M., Cazzani, A.M.: Contact interactions in complex fibrous metamaterials. *Continuum Mech. Thermodyn.* **33**(4), 1873–1889 (2021)
45. Spagnuolo, M., Peyre, P., Dupuy, C.: Phenomenological aspects of quasi-perfect pivots in metallic pantographic structures. *Mech. Res. Commun.* **101**, 103415 (2019). <https://doi.org/10.1016/j.mechrescom.2019.103415>
46. Ciallella, A., Pasquali, D., D’Annibale, F., Giorgio, I.: Shear rupture mechanism and dissipation phenomena in bias-extension test of pantographic sheets: numerical modeling and experiments. *Math. Mech. Solids* **27**(10), 2170–2188 (2022)
47. De Angelo, M., Barchiesi, E., Giorgio, I., Abali, B.E.: Numerical identification of constitutive parameters in reduced-order bi-dimensional models for pantographic structures: application to out-of-plane buckling. *Arch. Appl. Mech.* **89**(7), 1333–1358 (2019)
48. Shekarchizadeh, N., Abali, B.E., Barchiesi, E., Bersani, A.M.: Inverse analysis of metamaterials and parameter determination by means of an automatized optimization problem. *ZAMM-Zeitschrift für Angewandte Mathematik und Mechanik* **101**(8), 202000277 (2021)
49. Giorgio, I., Della Corte, A., dell’Isola, F., Steigmann, D.J.: Buckling modes in pantographic lattices. *Comptes rendus Mécanique* **344**(7), 487–501 (2016)
50. Ciallella, A., Steigmann, D.J.: Unusual deformation patterns in a second-gradient cylindrical lattice shell: numerical experiments. *Math. Mech. Solids*, 10812865221101820 (2022)
51. Maurin, F., Greco, F., Desmet, W.: Isogeometric analysis for nonlinear planar pantographic lattice: discrete and continuum models. *Continuum Mech. Thermodyn.* **31**(4), 1051–1064 (2019)
52. Greco, L., Cuomo, M., Contraffatto, L.: A reconstructed local B formulation for isogeometric Kirchhoff-Love shells. *Comput. Methods Appl. Mech. Eng.* **332**, 462–487 (2018)
53. Greco, L., Cuomo, M.: An implicit G^1 -conforming bi-cubic interpolation for the analysis of smooth and folded Kirchhoff-Love shell assemblies. *Comput. Methods Appl. Mech. Eng.* **373**, 113476 (2021)
54. Greco, L., Scrofani, A., Cuomo, M.: A non-linear symmetric G^1 -conforming Bézier finite element formulation for the analysis of Kirchhoff beam assemblies. *Comput. Methods Appl. Mech. Eng.* **387**, 114176 (2021)
55. Steigmann, D.J.: Equilibrium of elastic lattice shells. *J. Eng. Math.* **109**(1), 47–61 (2018)
56. Giorgio, I., Rizzi, N.L., Andreaus, U., Steigmann, D.J.: A two-dimensional continuum model of pantographic sheets moving in a 3D space and accounting for the offset and relative rotations of the fibers. *Math. Mech. Complex Syst.* **7**(4), 311–325 (2019)
57. dell’Isola, F., Seppecher, P., Della Corte, A.: The postulations á la D’Alembert and á la Cauchy for higher gradient continuum theories are equivalent: a review of existing results. *Proceed. Royal Soc. A: Math. Phys. Eng. Sci.* **471**(2183), 20150415 (2015)
58. Auffray, N., dell’Isola, F., Eremeyev, V.A., Madeo, A., Rosi, G.: Analytical continuum mechanics á la Hamilton-Piola least action principle for second gradient continua and capillary fluids. *Mathematics and Mechanics of Solids* **20**(4), 375–417 (2015)
59. Fedele, R.: Piola’s approach to the equilibrium problem for bodies with second gradient energies. Part I: First gradient theory and differential geometry. *Continuum Mech. Thermodynam.* **34**(2), 445– 474 (2022)
60. Spagnuolo, M., Yildizdag, M.E., Andreaus, U., Cazzani, A.M.: Are higher-gradient models also capable of predicting mechanical behavior in the case of wide-knit pantographic structures? *Math. Mech. Solids* (2020). <https://doi.org/10.1177/1081286520937339>
61. Hild, F., Misra, A., dell’Isola, F.: Multiscale DIC applied to pantographic structures. *Exp. Mech.* (2020)
62. dell’Isola, F., Turco, E., Misra, A., Vangelatos, Z., Grigoropoulos, C., Melissinaki, V., Farsari, M.: Force-displacement relationship in micro-metric pantographs: experiments and numerical simulations. *Comptes Rendus Mécanique* **347**(5), 397–405 (2019)
63. Spagnuolo, M., Yildizdag, M.E., Pinelli, X., Cazzani, A., Hild, F.: Out-of-plane deformation reduction via inelastic hinges in fibrous metamaterials and simplified damage approach. *Math. Mech. Solids* **27**(6), 1011–1031 (2022)
64. Auger, P., Lavigne, T., Smaniotto, B., Spagnuolo, M., dell’Isola, F., Hild, F.: Poynting effects in pantographic metamaterial captured via multiscale DVC. *J. Strain Anal. Eng. Design* **56**(7), 462–477 (2021)
65. Laudato, M., Barchiesi, E.: Non-linear dynamics of pantographic fabrics: modelling and numerical study. In: *Wave Dynamics. Mechanical Physical Microstructure Metamaterials*, pp. 241–254. Springer, Cham (2019)
66. Laudato, M., Manzari, L.: Linear dynamics of 2D pantographic metamaterials: numerical and experimental study. In: *Developments and Novel Approaches in Biomechanics and Metamaterials*, pp. 353– 375. Springer, Cham (2020)
67. Laudato, M., Manzari, L., Barchiesi, E., Di Cosmo, F., Göransson, P.: First experimental observation of the dynamical behavior of a pantographic metamaterial. *Mech. Res. Commun.* **94**, 125–127 (2018)
68. Turco, E., Barchiesi, E., dell’Isola, F.: A numerical investigation on impulse-induced nonlinear longitudinal waves in pantographic beams. *Math. Mech. Solids* **27**(1), 22–48 (2022)

69. Turco, E., Barchiesi, E., Ciallella, A., dell'Isola, F.: Nonlinear waves in pantographic beams induced by transverse impulses. *Wave Motion*, 103064 (2022)
70. Solyaev, Y., Babaytsev, A., Ustenko, A., Ripetskiy, A., Volkov, A.: Static and dynamic response of sandwich beams with lattice and pantographic cores. *J. Sandwich Struct. Mater.* **24**(2), 1076–1098 (2022)
71. Eugster, S.R.: Numerical analysis of nonlinear wave propagation in a pantographic sheet. *Math. Mech. Complex Syst.* **9**(3), 293–310 (2022)
72. Tornabene, F., Fantuzzi, N., Baccocchi, M.: Free vibrations of free-form doubly-curved shells made of functionally graded materials using higher-order equivalent single layer theories. *Compos. B Eng.* **67**, 490–509 (2014)
73. Fantuzzi, N., Tornabene, F., Baccocchi, M., Dimitri, R.: Free vibration analysis of arbitrarily shaped functionally graded carbon nanotube-reinforced plates. *Compos. B Eng.* **115**, 384–408 (2017)
74. Erden Yildizdag, M., Placidi, L., Turco, E.: Modeling and numerical investigation of damage behavior in pantographic layers using a hemivariational formulation adapted for a Hencky-type discrete model. *Continuum Mech. Thermodynam.*, 1–14 (2022)
75. Spagnuolo, M., Barcz, K., Pfaff, A., dell'Isola, F., Franciosi, P.: Qualitative pivot damage analysis in aluminum printed pantographic sheets: numerics and experiments. *Mech. Res. Commun.* **83**, 47–52 (2017)
76. Amar, M., Chiricotto, M., Giacomelli, L., Riey, G.: Mass-constrained minimization of a one-homogeneous functional arising in strain-gradient plasticity. *J. Math. Anal. Appl.* **397**(1), 381–401 (2013)
77. De Angelo, M., Spagnuolo, M., D'Annibale, F., Pfaff, A., Hoschke, K., Misra, A., Dupuy, C., Peyre, P., Dirrenberger, J., Pawlikowski, M.: The macroscopic behavior of pantographic sheets depends mainly on their microstructure: experimental evidence and qualitative analysis of damage in metallic specimens. *Continuum Mech. Thermodynam.* **31**(4), 1181–1203 (2019)
78. Placidi, L., Timofeev, D., Maksimov, V., Barchiesi, E., Ciallella, A., Misra, A., dell'Isola, F.: Micro-mechano-morphology-informed continuum damage modeling with intrinsic 2nd gradient (pantographic) grain-grain interactions. *Int. J. Solids and Struct.* **254**, 111880 (2022)
79. Valmalle, M., Vintache, A., Smaniotto, B., Gutmann, F., Spagnuolo, M., Ciallella, A., Hild, F.: Local-global DVC analyses confirm theoretical predictions for deformation and damage onset in torsion of pantographic metamaterial. *Mech. Mater.*, 104379 (2022)
80. Cuomo, M., Contrafatto, L., Greco, L.: A variational model based on isogeometric interpolation for the analysis of cracked bodies. *Int. J. Eng. Sci.* **80**, 173–188 (2014)
81. Battista, A., Rosa, L., dell'Erba, R., Greco, L.: Numerical investigation of a particle system compared with first and second gradient continua: Deformation and fracture phenomena. *Math. Mech. Solids* **22**(11), 2120–2134 (2017)
82. Ciallella, A., Pasquali, D., Gołaszewski, M., D'Annibale, F., Giorgio, I.: A rate-independent internal friction to describe the hysteretic behavior of pantographic structures under cyclic loads. *Mech. Res. Commun.* **116**, 103761 (2021)